Soft Matter

PAPER

View Article Online
View Journal | View Issue

Cite this: *Soft Matter*, 2020, **16**, 6091

Hydrogen bonding and charge transport in a protic polymerized ionic liquid†

Arthur Markus Anton, *[ab] Falk Frenzel, [a] Jiayin Yuan, [c] Martin Tress [ad] and Friedrich Kremer [a]

Received 25th February 2020,
Accepted 7th June 2020

DOI: 10.1039/d0sm00337a

rsc.li/soft-matter-journal

Hydrogen bonding and charge transport in the protic polymerized ionic liquid poly[tris(2-(2-methoxyethoxy)ethyl)ammoniumacryloxypropyl sulfonate] (PAAPS) are studied by combining Fourier transform infrared (FTIR) and broadband dielectric spectroscopy (BDS) in a wide temperature range from 170 to 300 K. While the former enables to determine precisely the formation of hydrogen bonds and other moiety-specific quantized vibrational states, the latter allows for recording the complex conductivity in a spectral range from 10^{-2} to 10^{+9} Hz. A pronounced thermal hysteresis is observed for the H-bond network formation in distinct contrast to the reversibility of the effective conductivity measured by BDS. On the basis of this finding and the fact that the conductivity changes with temperature by orders of magnitude, whereas the integrated absorbance of the N–H stretching vibration (being proportional to the number density of protons in the hydrogen bond network) changes only by a factor of 4, it is concluded that charge transport takes place predominantly due to hopping conduction assisted by glassy dynamics (dynamic glass transition assisted hopping) and is not significantly affected by the establishment of H-bonds.

1 Introduction

Polymerized ionic liquids (polyILs) form a unique class of electrolyte materials, which combines the favorable properties of neat ionic liquids (ILs), such as ion conductivity,[1] wide electrochemical and thermal stability,[2,3] or non-flammability,[4] with the macromolecular benefits of polymers like mechanical stability.[5,6] Based on the polyILs' properties they can be used in multifold applications, such as solvents,[7,8] in electro- and biochemistry,[9,10] engineering,[11] or aeronautics.[12] Among the wide field of ILs, protic ionic liquids (proILs) represent a subset produced through combining a Brønsted acid with a Brønsted base.[13] Because of the proton transfer from the acid to the base, proton donor and acceptor sites are present, which are well suited to form hydrogen bonds (H-bonds). One consequence of this is that the amount of hydrogen bonds within the sample can significantly affect the polyIL's macroscopic properties.[14–17] It can be demonstrated that water added to a protic polyIL acts as plasticizer and reduces the (calorimetric) glass transition temperature (T_g) as well as it increases the DC-conductivity at absolute temperatures.[18,19]

Another strategy to modify the polyILs' conductivity behavior is to place a spacer unit at the IL-like side group attached to the polymer backbone or between the backbone and the IL-like group.[20–24] This architecture reduces T_g with increasing spacer length with the result of an increased DC-conductivity at absolute temperatures for the most cases, but a lowered DC-conductivity at T_g-normalized temperatures (T/T_g) for all cases. The same holds true for increasing the size of the counterion.[22]

For the most (but not all) cases the mechanism of charge transport in non-crystalline polyILs (as well as low molecular weight ILs) can be comprehended as class transition assisted hopping.[25–27] In this model hopping of charges is governed by molecular fluctuations, and consequently the conductivity of the materials is predominantly determined by the dynamics of the glassy system.[28] This is in particular evidenced by the proportionality between the hopping rate of the charge carriers and relaxation rate of thermally activated fluctuations obeying glassy dynamics. Moreover, this relation can typically be observed

[a] *Leipzig University, Peter Debye Institute for Soft Matter Physics, Linnéstraße 5, 04103 Leipzig, Germany. E-mail: a.m.anton@outlook.de*
[b] *The University of Sheffield, Department of Physics and Astronomy, Hicks Building, Hounsfield Road, Sheffield S3 7RH, UK*
[c] *Stockholm University, Department of Materials and Environmental Chemistry, Svante Arrhenius väg 16C, 106 91 Stockholm, Sweden*
[d] *University of Tennessee, Department of Chemistry, 1420 Circle Drive, Knoxville, Tennessee 37996, USA*

† Electronic supplementary information (ESI) available: Analysis of possible H-bond sites, hysteresis of σ′ for a wider frequency range, FTIR spectra of additional samples for comparison measurements and peak assignments, FTIR spectra of $\nu_{as}((SO_3))$, FTIR spectra and further analysis of $\nu((N–H))$, FTIR spectra and analysis of $\nu((C{=}O))$, FTIR spectra and analysis of $\rho_{gauche}((CH_3))$, $\nu_{trans\text{-}gauche}((CH_3))$ and $\nu_{as}((C–O–C))$, correlation between the different analyzed vibrational modes and ^{1}H NMR spectra of the polyIL PAAPS and the monomer AAPS. See DOI: 10.1039/d0sm00337a

over 6 to 8 orders of magnitude and holds true for both low molecular weight ILs[29,30] as well as polymeric systems.[27,31,32]

Recently, Gainaru *et al.* and Stacy *et al.* published a model for a direct estimate of ion diffusion on the basis of the conductivity relaxation process and further a qualitative model describing ionic transport as a competition between electrostatic and elastic forces, respectively. In addition to the correlation with the ion size, which determines the particular regime (electrostatic or elastic), the authors suggested an increase of the dielectric permittivity in order to reduce T_g and the energy barrier for small ion conductivity.[33,34]

In the current manuscript we study the sample material poly[tris(2-(2-methoxyethoxy)ethyl)ammonium acryloxypropyl sulfonate] (PAAPS), which exhibits one of the highest values of DC-conductivity at room temperature for anhydrous (water-free) polymer systems as recently reported in our previous work.[31] Even though this material makes use of a reduced T_g by an increased side chain length and counterion size, PAAPS appears highly viscous at room temperature.[35] In order to investigate the mechanism of charge transport in this promising material in detail on the molecular scale, we examine a combination of temperature-dependent Fourier transform infrared (FTIR) and broadband dielectric spectroscopy (BDS). Even though FTIR and BDS measurements are routinely employed as separate methods in order to study (poly)ILs, combining them is very uncommon. However, this combination enables us, on the one hand, to follow the temperature-dependent evolution of the macroscopic complex conductivity, and on the other hand, to assess alterations of moiety-specific molecular vibrations.

We follow the formation and deterioration of an extended H-bond network during a cooling-heating cycle. A detailed analysis reveals that the network remains intact during heating giving rise to a pronounced hysteresis, which allows for comparing the DC-conductivity of the identical sample at the same temperature with a tremendous difference in H-bond density. Surprisingly and contrary to the concept of fast proton hopping,[17,36] in the case of PAAPS, H-bond formation hinders charge transport. We discuss the charge transport mechanism which is governed by thermally activated molecular fluctuations, whereas hydrogen bonding hinders fluctuations and thus reduces the DC-conductivity. These novel results about which moieties are involved in inter-molecular binding on the microscopic scale and how H-bonds affect the macroscopic conductivity for the particular case of PAAPS suggest a reassessment of the role of H-bonds for conductivity.

2 Materials and methods

2.1 Sample material

The synthesis of the sample material poly[tris(2-(2-methoxyethoxy)ethyl)ammonium acryloxypropyl sulfonate] (PAAPS) has been published by Prescher *et al.*[35] and Frenzel *et al.*,[31] in the former for the repeat unit and in the latter for the polymerized ionic liquid (polyIL, Fig. 1), respectively. The molecular weight of the examined sample was M_n = 99 500 g mol^{-1}.

2.2 Temperature- and frequency-dependent broadband dielectric spectroscopy

For broadband dielectric spectroscopy (BDS) two devices have been used; in the frequency range of $f = 10^{-2}$–10^{+7} s^{-1} a high-resolution α-analyzer (Novocontrol Technologies GmbH & Co. KG, Germany) and in a range of $f = 10^{+7}$–10^{+9} s^{-1} a 4291A impedance/material analyzer and a high impedance test head (Hewlett Packard, USA). Both spectrometers are equipped with a Quatro temperature controller (temperature accuracy ≤1 K, (Novocontrol Technologies GmbH & Co. KG, Germany)). In the case no error bars are provided, the measurement uncertainty is smaller than the symbol size.

Sample cells dedicated to be measured in the first device consisted of a polished brass electrode (40 mm diameter), glass fibers (50 μm diameter) acting as spacers, and a second polished brass electrode (10 mm diameter). In order to remove as much water as possible, a droplet of PAAPS has been placed on the bigger, lower electrode with glass fibers on top and stored at 423 K in high vacuum (10^{-6} mbar) for at least 12 hours. The smaller, upper electrode has not been placed on top of the sample yet, but experienced the same temperature and atmospheric treatment as the rest of the sample. After the temperature and vacuum treatment, the vacuum chamber was flushed with Argon and the hot upper electrode was put on top of the hot sample, forming the capacitor for the BDS measurements. Dielectric spectra have been recorded from 300 K down to 170 K and back in steps of 5 K with an effective cooling/heating rate of 5×10^{-5} K s^{-1}.

Samples for the high frequency spectrometer were composed of two gold coated brass electrodes (5 mm diameter), two thin Teflon stripes (520 μm thickness) acting as spacers, and a Teflon ring slightly wider than the electrodes in order to hold this arrangement in place. Spectra have been recorded under dry nitrogen atmosphere in the temperature range from 310 K to 170 K and back in steps of 5 K with a cooling/heating rate of 5 K s^{-1}.

2.3 Temperature-dependent infrared spectroscopy

Infrared (IR) spectra have been recorded by means of a Bio-Rad FTS 6000 FTIR spectrometer equipped with a UMA 500 IR microscope and a liquid nitrogen-cooled mercury–cadmium–telluride (MCT) detector (Kolmar Technologies, Inc., USA). The sample temperature has been controlled using a THMS 350V stage (Linkam Scientific Instruments, UK) flushed with dry nitrogen. IR spectra have been recorded from 300 K down to 170 K and back in steps of 5 K with an effective cooling/heating rate of 0.012 K s^{-1}.

Samples for IR spectroscopy have been prepared by dissolving the sample material in deionized water (18.2 MΩ cm^{-1}, Milli-Q, Merck, Germany) and drop-casting the solution on an IR-transparent substrate (BaF_2, Korth Kristalle GmbH, Germany). This method facilitates the adjustment of the sample thickness by subsequent dropping and drying until the desired absorption is reached. Afterward the sample films have been stored at 423 K in vacuum (10^{-6} mbar) for at least 12 hours, in order to remove the water used for preparation and absorbed from ambient air.

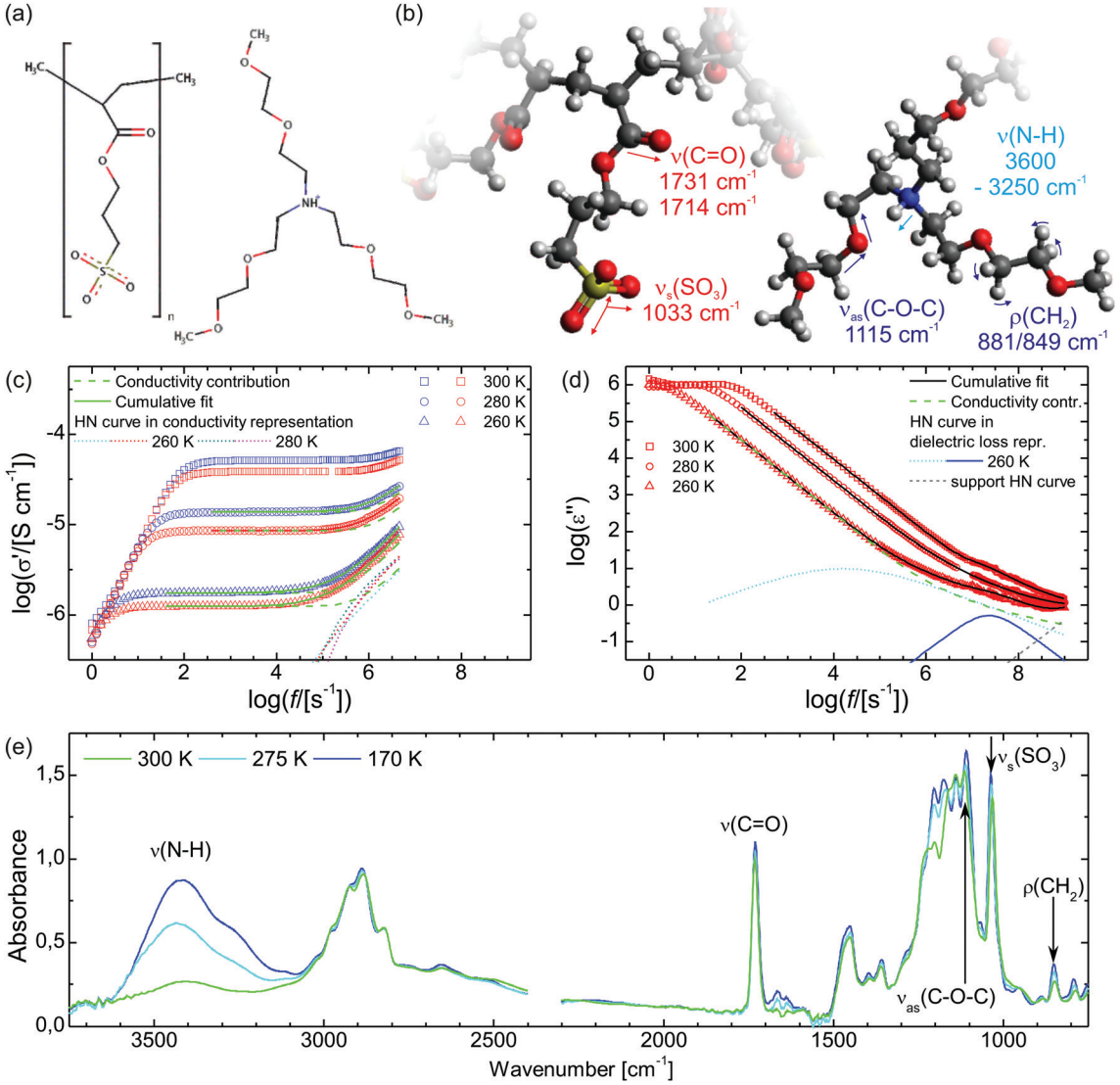

Fig. 1 (a) The chemical structure of the polymerized ionic liquid (polyIL) PAAPS and (b) its molecular vibrations along with their mean frequencies ($\nu_{(s/as)}$: (symmetric/antisymmetric) stretching vibration; ρ: rocking vibration). (c) The real part σ' of the complex conductivity $\sigma^* = \sigma' + i\sigma''$ and (d) the imaginary part ε'' of the complex dielectric function $\varepsilon^* = \varepsilon' - i\varepsilon''$ as measured by means of broadband dielectric spectroscopy (BDS). The blue and red symbols indicate the cooling run from 300 K to 170 K and the heating run form 170 K back to 300 K, respectively. An offset between the plateaus of the DC-conductivity at the same temperature during the cooling and heating run is evident. (e) FTIR spectra of PAAPS at different temperatures; absorption bands used for structural analyses are indicated. The logarithm in panels c and d is to base 10. The measurement uncertainty is smaller than the symbol size.

The sample has been transported in dry argon atmosphere and measured in dry nitrogen atmosphere.

3 Results

3.1 Broadband dielectric spectroscopy

A basic study on the sample's dielectric and conductive properties has been published previously.[31] Therein, dielectric relaxation processes and conductivity has been studied in the frequency range from 10^{-2} to 10^{+7} s^{-1}. The primary α relaxation has been ascribed to fluctuations of transient dipole moments, whereas the secondary β relaxation to fluctuations of the carboxyl group. Furthermore, PAAPS emerged as a polyIL exhibiting one of the highest values of DC-conductivity at 300 K so far published for anhydrous (water-free) polyILs.[31,37] In order to investigate the mechanism of charge transport in detail, we expand the frequency range for BDS measurements up to 10^{+9} s^{-1} (Fig. 1). The detriment of the high DC-conductivity interfering with the primary relaxation process in dielectric loss spectra $\varepsilon''(\omega)$ is circumvented by fitting a superposition of a conductivity contribution and a relaxation process in the real part of the complex conductivity $\sigma'(\omega)$ (Fig. 1c).[38] In detail we make use of

$$\sigma^*(\omega) = i\omega\varepsilon_0\varepsilon^*, \quad (1)$$

where σ^*, ω, i, ε_0 and ε^* denote the complex conductivity with $\sigma^* = \sigma' + i\sigma''$, the angular frequency, the imaginary unit, the vacuum permittivity, and the complex dielectric function with

$\varepsilon^* = \varepsilon' - i\varepsilon''$, respectively. The complex conductivity can be expressed as

$$\sigma^*(\omega) = \sigma_0\left[\frac{i\omega\tau_e}{\ln(1+i\omega\tau_e)}\right] \quad (2)$$

with $\tau_e = 1/\omega_c$ representing the charge carrier hopping rate,[38] while relaxation processes are usually described by a single or a sum of Cole–Cole (CC) or Havriliak–Negami (HN) functions given through[25]

$$\varepsilon_{CC}{}^*(\omega) = \varepsilon_\infty + \frac{\Delta\varepsilon}{1+(i\omega\tau_{CC})^\beta} \quad (3)$$

$$\varepsilon_{HN}{}^*(\omega) = \varepsilon_\infty + \frac{\Delta\varepsilon}{\left[1+(i\omega\tau_{HN})^\beta\right]^\gamma}. \quad (4)$$

When fitting in the σ'-representation, on the one hand, the value of σ_0 can be directly obtained from the measured plateau level and, on the other hand, the increase of the AC-conductivity at higher frequencies is properly described through the random free-energy barrier model.[38,39] Consequently, the relaxation process in the measured curves (as sum of conductivity and relaxation) is accounted for by a CC function instead of the more general HN function,[40] because a CC function is symmetric and only one side of the relaxation process can be seen in the spectra.

The thus obtained mean relaxation times of this process confirm the extrapolation of values determined previously for the α-relaxation at lower temperatures (Fig. 2a).[31] Making use of the relaxation time for the α-relaxation $\tau_{\alpha\text{-CC}}$ as well as the values of the DC-conductivity σ_0 and critical frequency of the charge transport ω_c, the relaxation times for the secondary process (as HN function) are determined on the basis of a combination of dielectric loss spectra in the ε''-representation in the frequency ranges of 10^{-2} to 10^{+7} s^{-1} and 10^{+7} to 10^{+9} s^{-1} (Fig. 1d). The relaxation times for the secondary β-relaxation also agree with the values determined at lower temperatures (Fig. 2a).[31] When we approximate the thermal activation of the α- and β-relaxation times with a Vogel–Fulcher–Tammann (VFT) and an Arrhenius functions,[40] the rates of both processes are separated by less than 1 decade for $T_g/T \leq 0.74$ and do intersect at $T_g/T = 0.72$.

In the conductivity spectra (Fig. 1c), it is evident that the plateau of the DC-conductivity at a particular temperature is higher in the case of the cooling run as compared to the

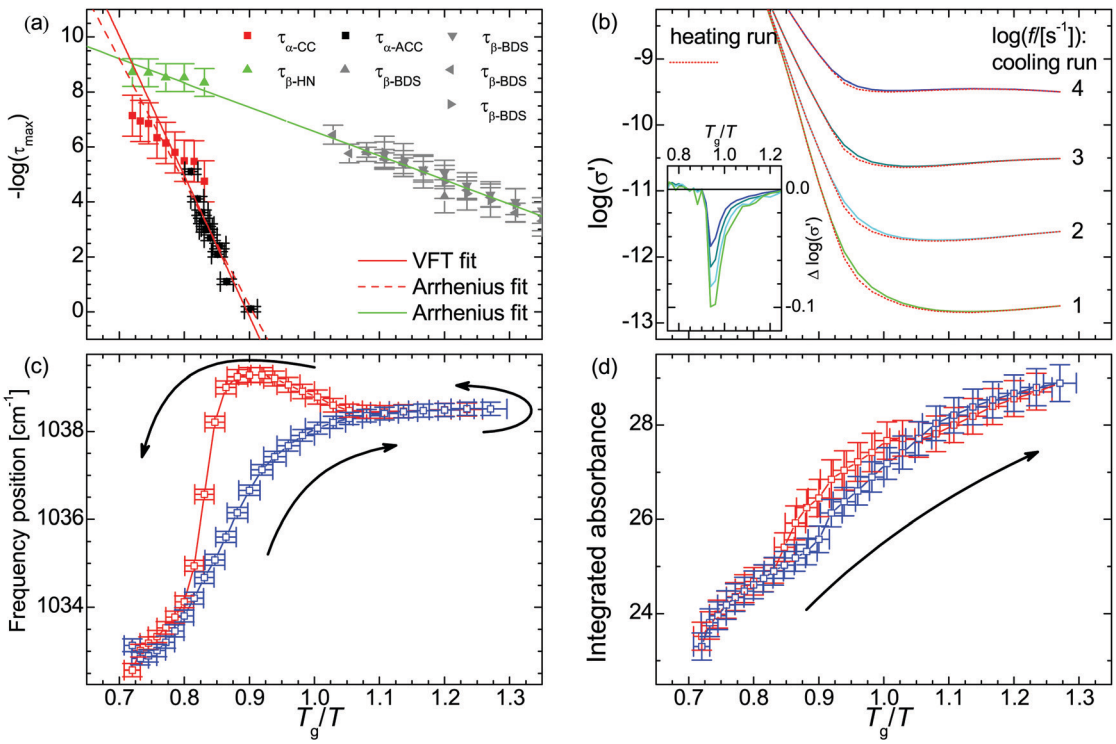

Fig. 2 (a) Relaxation time of the primary τ_α and secondary relaxation processes τ_β in PAAPS (red and green symbols: spectra measured using the described combination of normal and high frequency dielectric spectroscopy; $\tau_{\alpha\text{-CC}}$ primary relaxation derived in the σ'-representation using a Cole–Cole (CC) function; $\tau_{\beta\text{-HN}}$ secondary relaxation derived in the ε''-representation using a Havriliak–Negami (HN) function; black and grey symbols: spectra measured by means of BDS and alternating current chip calorimetry (ACC), data taken from Frenzel *et al.*, ref. 31; $\tau_{\alpha\text{-ACC}}$ primary relaxation derived by means of ACC; $\tau_{\beta\text{-BDS}}$ secondary relaxation derived by using a HN function in the normal frequency BDS range (10^{-2} to 10^{+7} s^{-1}); solid red line: VFT fit; solid green line and dashed red line: Arrhenius fits). (b) Real part σ' of the complex conductivity function depending on the inverse temperature scaled with the glass transition temperature T_g = 216 K. The inset depicts the difference between the cooling and heating run; at the same temperature σ_0 is up to 20% smaller during the heating run than during previous cooling. (c) Frequency position $\bar{\nu}$ and (d) integrated absorbance A_{int} of the symmetric SO_3 stretching vibration $\nu_s(SO_3)$. The blue and red symbols denote data recorded during the cooling run from 300 K to 170 K and the reversed heating, respectively. The logarithm in panels a and b is to base 10.

subsequent heating. Similarly, in the temperature-dependent representations of the conductivity spectra for particular frequencies (Fig. 2b), the decrease of the conductivity (because of cooling) takes place at lower temperatures (higher values of T_g/T) than the respective increase of conductivity during the subsequent heating run; we observe a hysteresis for the DC-conductivity. The maximum difference between the conductivity during the heating and previous cooling run is

$$\Delta \log_{10}(\sigma') = \log_{10}(\sigma')|_{\text{heating}} - \log_{10}(\sigma')|_{\text{cooling}} \quad (5)$$

$$= -0.10 \quad (6)$$

at $T_g/T = 0.94$ ($T = 230$ K), which resembles a reduction of σ_0 by 20% during the heating run as compared to that at the identical temperature during the cooling run. In order to ensure that we determine the hysteresis of the DC-conductivity we restrict the frequency range to $\log_{10}(f/[\text{s}^{-1}]) = 1$ to 5; for lower frequencies a more pronounces hysteresis can be observed (Fig. S2 in the ESI†).

3.2 Infrared spectroscopy

Within the IR spectra of PAAPS we identify absorption peaks and bands specific for charged and uncharged moieties within the polymer side chain as well as the cation (Table 1). Among them, the quaternary ammonium group is the only hydrogen bond donor; in contrast, the ether group in the cation as well as the carboxyl and sulfonate groups in the polymer side chains are hydrogen bond acceptors (determined by means of the Hydrogen Bond Donor/Acceptor Plugin in Mavin by ChemAxon, for further information see ESI,† Fig. S1). For the sake of conciseness, we will focus on the ammonium and sulfonate groups as main H-bond partners, as discussed below. For the other moieties the interested reader is referred to the ESI.†

3.2.1 SO_3 symmetric stretching vibration. The sulfite group (SO_3) at the outermost position of the polymer side chain gives rise to a prominent peak at $\bar{\nu} = 1033$ cm^{-1} (at 300 K), which represents the absorption arising from the symmetric stretching vibration of the SO_3 group ($\nu_s(SO_3)$), (Fig. 1, Fig. S6, ESI† and Table 1).[45–47] With decreasing temperature this peak is reversibly shifted to higher frequencies (Fig. 2c). In addition, the shift exhibits a pronounced hysteresis which sets in between $T_g/T = 1.10$–1.05 ($T = 196$–206 K); a temperature which matches well with the glass transition temperature of the repeat unit (RU, comprising one monomer and one cation) ($T_g^{RU} = 199$ K, $T_g/T_g^{RU} = 1.09$).[35] The glass transition temperature of the polymer, instead, is higher than that of the repeat unit ($T_g^{pol} = 216$–225 K, $T_g/T_g^{pol} = 1.00$–0.96)[31,35] and lies inbetween the commencement of the hysteresis and the temperature of its maximum value. Please note, the calorimetric glass transition temperature of $T_g = 216$ K determined by means of differential scanning calorimetry (DSC) has been used throughout this work to scale the diagrams. Other methods as BDS or AC-chip calorimetry lead to slightly different values of T_g,[31] which explains the range of values for T_g/T_g^{pol} provided above.

From the chemical structure it is evident that the sulfonate part is negatively charged with oxygen as a standard hydrogen bond acceptor (Fig. S1, ESI†). Consequently, we expect that the sulfonate group is an H-bond acceptor. In general, when a stretching vibration undergoes hydrogen bonding, the respective peak frequency is reduced (red shift) due to weakening of covalent bonds, whereas the band intensity is enhanced.[55] However, in the particular case of $\nu_s(SO_3)$ the band intensity increases during hydrogen bonding while the frequency exhibits a blue shift (instead of a red shift). This indicates binding of one N–H group to one oxygen atom of the sulfonate group as described by Huang *et al.* (monodentate ion pairs as well as bi- and tridentate bridges are causing a blue shift, while bi- and tridentate ion pairs are causing a red shift).[48] A blue shift arising from hydrogen bonding is also found for $\nu_s(SO_3)$ in ethyl sulfate.[56] Additionally, this 1 : 1 donor : acceptor ratio can also be found in the case of the proIL ethylammonium hydrogen sulfate exhibiting a similar chemical structure of donor and acceptor.[57]

Furthermore, the temperature of the maximum hysteresis of the IR blue shift coincides with the maximum of $\Delta \log(\sigma')$ (eqn (5), inset in Fig. 2b). Thus, the onset of the hysteresis at T_g^{RU} indicates that already at this temperature the polymer side chains are mobile enough for structural reorganization. In addition, the maximum of the hysteresis and its concordance with the most reduced conductivity at a particular temperature indicate that in PAAPS, hydrogen bonding hinders charge transport.

We want to emphasize that this pronounced hysteresis is observed despite of the very small effective cooling/heating rate of 0.012 K s^{-1} throughout the whole measurement. At this rate it takes 100 s to change the temperature by about 1 K, which is accepted as the rate of structural relaxations at the dynamic glass transition temperature.[31,32] This means that at any temperature above T_g the system can easily equilibrate and effects of thermal or dynamic inertia are excluded.

3.2.2 N–H stretching vibration. At higher wavenumbers the prominent band of the N–H stretching vibration arises with decreasing temperature ($\bar{\nu} = 3600$–3250 cm^{-1}, Fig. 1, Fig. S7, ESI† and Table 1), which is a combination of peaks indicative of hydrogen bonding.[58]

In order to unravel the temperature dependence of the hydrogen bonding of the of N–H moiety, 4 Gaussian (plus 1 for the adjacent band at the low wavenumber side) are fitted to this band and their integrated absorbance (A_{int}) measured by the area under the curve (AuC) is recorded (Fig. 3 and Fig. S7, S8, ESI†). When the temperature is decreased to 170 K, the cumulative AuC (sum of the AuCs of the particular peaks)

Table 1 Peaks and bands employed for structure elucidation. The frequency position denotes values at 300 K. For more details see ESI Fig. S4 and S5

Frequency position $\bar{\nu}$, [cm^{-1}]	Assignment	Abbreviation	Ref.
881/849	CH_2 rocking	$\rho(CH_2)$	41–44
1033	SO_3 symmetric stretching	$\nu_s(SO_3)$	45–50
1115	C–O–C antisymmetric stretching	ν_{as}(C–O–C)	42 and 51
1731/1713	C═O stretching, free/bound	$\nu_{f/b}$(C═O)	52 and 53
3400–3250	N–H stretching	ν(N–H)	50 and 54

increases up to the 8.6-fold of the initial value at 300 K, which quantifies the increase of the number density of hydrogen bonds. (The cumulative AuC is chosen, because this is the most reliable measure. Due to the minor structure of this band, individual peak positions may vary and hence the individual AuCs are affected.) During the subsequent heating the number density increases even further to the 10.3-fold at T_g/T = 0.90 (240 K). Only then, further heating leads to a reduction of the hydrogen bond density and eventually the initial value at 300 K is recovered. In order to exclude that the variation in the occupation of states causes the altered band intensity, we estimate the populations via a Boltzmann distribution. We find that for all peaks the ratio of the population in the first excited state to the population of the ground state is $\leq 3 \times 10^{-7}$ at 300 K, and $\leq 3 \times 10^{-12}$ at 170 K. Thus, already at 300 K the first (and any higher excited state) is effectively unoccupied and the absorption is not affected by the variation in the population numbers.

In the trajectory of the AuC two kinds of traces can be identified in the set of absorption peaks assigned to the N–H stretching vibration. On the one hand, there are peaks undergoing a two-step hysteresis during heating (Fig. 3b and Fig. S8b, d, ESI†). In the case of these peaks, the hysteresis sets in immediately after the lowest temperature of 170 K has been passed and the sample is heated (Fig. 3b). This clearly indicates remaining molecular mobility, even though the system is at 46 K below the macroscopic glass transition temperature T_g.[31,35] On the other hand, there are peaks undergoing a one-step hysteresis during heating (Fig. 3d and Fig. S8f, h, ESI†), similar to the frequency position of $\nu_s(SO_3)$ (Fig. 2c). For these peaks, the hysteresis does not start right with the beginning of the heating run at 170 K but still before T_g is reached, namely at T_g^{RU} as in the case of $\nu_{as}(SO_3)$.

3.2.3 Correlation between vibrational modes. In order to clarify the interaction of molecular moieties, we prepare a correlation-plot with the apparent temperature as parameter (Fig. 4). Therefor, we use the fact that the frequency shift and the integrated absorbance depend linearly and to the power of 1/2 on the H-bond enthalpy, respectively.[58,59] On the one hand, Iogansen discussed in detail that the AuC can be determined more precisely than the position of the ν(N–H) peak,[58] even for a well-separated peak. Because for PAAPS the ν(N–H) band appears complexly structured, the cumulative AuC is the most reliable measure. On the other hand, Zhang *et al.* analyzed the frequency shift and the molar absorbance of $\nu_s(SO_3)$.[56] The authors stated, that a reduction of the number of hydrogen bonds leads to monotonous decrease of the peak frequency while the molar absorbance, instead, showed a maximum. Thus, we concentrate on the frequency position of $\nu_s(SO_3)$, which can precisely be determined due to the narrow and solitary peak. In the respective plot ($\bar{\nu}(SO_3)$ *vs.* $A_{int}(N–H)^{1/2}$, Fig. 4) the individual data points represent different temperatures during the cooling and heating run and form a fairly straight line. The strong correlation suggests that the H-bonds are mainly formed between the SO_3 moiety of the polymer side chain and the N–H group of the cation. Even the hysteresis during the heating run evident as point cloud at $A_{int}^{1/2} \approx 18$ cm$^{-1/2}$

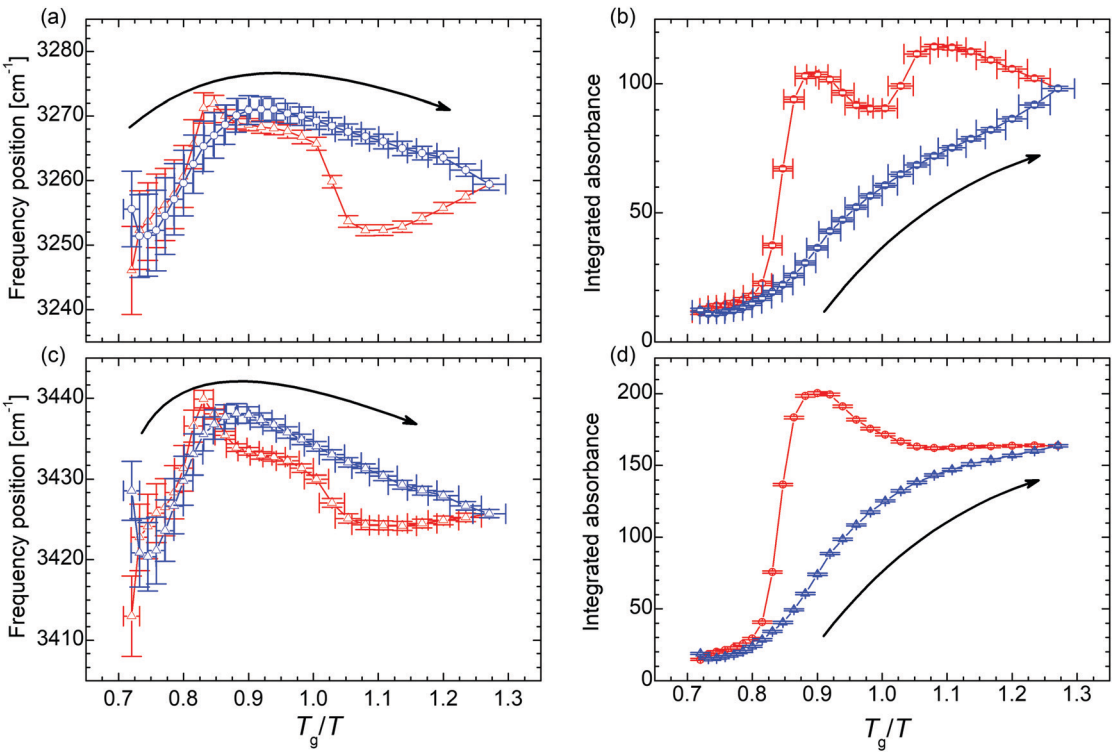

Fig. 3 (a) and (c) Temperature dependence of the frequency position and (b) and (d) integrated absorbance of the N–H stretching vibration ν(N–H). The blue symbols denote data points recorded during the cooling run, the red symbols during the subsequent heating run. The arrows indicate the direction of the initial cooling. The analysis of the remaining N–H stretching peaks can be found in the ESI.†

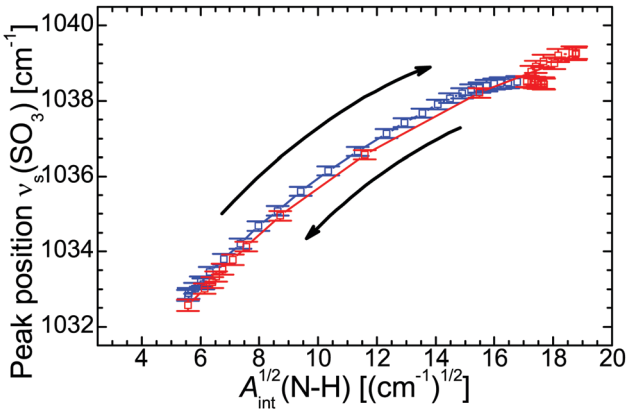

Fig. 4 Correlation between the temperature-induced alteration of $\nu_s(SO_3)$ *vs.* ν(N–H).

coincides with the approximately linear correlation. Other significant interactions with the N–H group, for example with the C–O–C moiety, can be excluded on the basis of the according correlation plots (see ESI†).

4 Discussion

4.1 Proton Transfer

One measure to discern between ILs and a mixture of ionic and neutral species is the difference between the aqueous pK_a values of the base and the acid,

$$\Delta pK_a = pK_a(\text{base}) - pK_a(\text{acid}). \quad (7)$$

The bigger ΔpK_a, the more favored is the proton transfer.[13,60] When ΔpK_a is rather small, a non-complete proton transfer is indicated and neutral, non conducting moieties are present. Belieres and Angell proposed $\Delta pK_a \geq 10$ for highly ionized proILs,[61] whereas MacFarlane *et al.* derived that $\Delta pK_a \approx 4$ is sufficient for complete proton transfer.[62] Recently, Wojnarowska *et al.* published proILs with proton conduction exhibiting ΔpK_a values from 3.2 to 6.0.[36] In the case of PAAPS we determine $\Delta pK_a = 9.0$ (by means of Mavin by ChemAxon), which implies high proton transfer and the formation of a highly ionized proIL.

Davidowski *et al.*[63] employed NMR spectroscopy in order to characterize the ionicity and transport properties of a series of proILs formed by protonation of diethylmethylamine. The charged center of this molecule is fairly comparable with that of the cation in PAAPS. From the ^{1}H chemical shift, the authors deduced the affinity of the proton to the base. For PAAPS and AAPS we found a chemical shift of 9.3 and 9.1 ppm (Fig. S13 in the ESI†), respectively. On the basis of the calibration line elaborated by Davidowski *et al.* (Fig. 3 in ref. 63), we further calculate a proton affinity of 318 kcal mol^{-1} (13.8 eV) and 317 kcal mo^{-1} (13.8 eV), respectively. In addition Davidowski *et al.* derived a correlation between the ^{1}H chemical shift and ΔpK_a (Fig. 2 in ref. 63). According to this correlation the ΔpK_a values for PAAPS and AAPS are supposed to amount to 12.0 and 12.5, respectively. However, Davidowski *et al.* stated that the proton chemical shift is a better predictor for the proton transfer than the frequently used ΔpK_a values.

In the following discussion we will show that these values of the chemical shift correspond to a partial proton transfer. This means, the proton is neither completely at the donor, nor at the acceptor site; it is bridging both moieties.[63]

With regard to Nakamoto *et al.* the different N–H bond distances can be approximated from the particular $\bar{\nu}$(N–H).[64] On the basis of the derived parameters for the different peaks, the values of the N–H···O bond length are between 2.9 and 3.2 Å, whereas each bond does not change by more than 0.02 Å during the temperature cycle. Thus, we treat this distance as constant during the measurement. This is corroborated by DFT simulations (ORCA program system, B3LYP/6-31G(d) and B3LYP/6-31G(2d,2p)[65–69]) yielding a distance of 2.6 Å (d(N–H) = 1.1 Å and d(H···O) = 1.5 Å; literature, Hayes *et al.* d(H···O) = 1.6 Å[57]) for the relaxed structure of one repeat unit and one anion *in vacuo*. Further repeat units and additional anions may introduce structural constraints and increase the bond distance.

4.2 Charge transfer mechanism

The chemical structure of the H-bonding moieties of PAAPS (center of the cation and sulfate group at the outermost position at the polymer side chain) is similar to that in DEMA-MS (mixture of diethylmethylamine with methanesulfonic acid), a sample studied by Davidowski *et al.*[63] Interestingly, both PAAPS as well as DEMA-MS show a comparable chemical shift of the exchangeable proton (9.3/9.1 *vs.* 9.5 ppm), and thus a comparable proton affinity to the base. In addition, ^{15}N pulsed-field gradient NMR spectroscopy on DEMA-MS revealed that anion, cation, and exchangeable proton diffuse with the same rates, which is why the authors presumed a "hydrogen bonded ion pair".[63] On the basis of our IR spectroscopy results and the similar chemical structures of the hydrogen bond donor and acceptor in the cases of PAAPS/AAPS and DEMA-MS, we validate the existence of an extended hydrogen bond network. Moreover, the comparable diffusion constants of anion, cation, and exchangeable proton as determined by Davidowski *et al.*[63] corroborate our findings of a correlation between the rates of structural fluctuation (α-relaxation) and charge transport (ω_c) as determined by Frenzel *et al.*[31] Thus, the mechanism of charge transport can indubitably be specified as a hopping mechanism strongly influenced through the glassy nature of the polymeric system (known as glass transition assisted hopping conduction).[27,31,32,70] This means, hopping depends on the thermally activated fluctuations of molecules, which are drastically slowed down at the dynamic glass transition. Thus, the dynamic behavior of the glass building polymer influences molecular mobility and hence the events of hopping.[27,70]

Further verification of the glass transition assisted hopping conduction mechanism is provided by the thermal response of PAAPS. Therefor, we divide the evolution of H-bonding and DC-conductivity during the temperature cycle into 4 steps (Fig. 5); first, cooling from 300 K to 240 K (T_g/T = 0.90), the latter of which is the temperature of the maximum hysteresis; second, cooling from 240 K to 170 K (T_g/T = 1.27) *i.e.* the lowest recorded temperature; and third and fourth, subsequent heating to 240 K and further to 300 K, respectively.

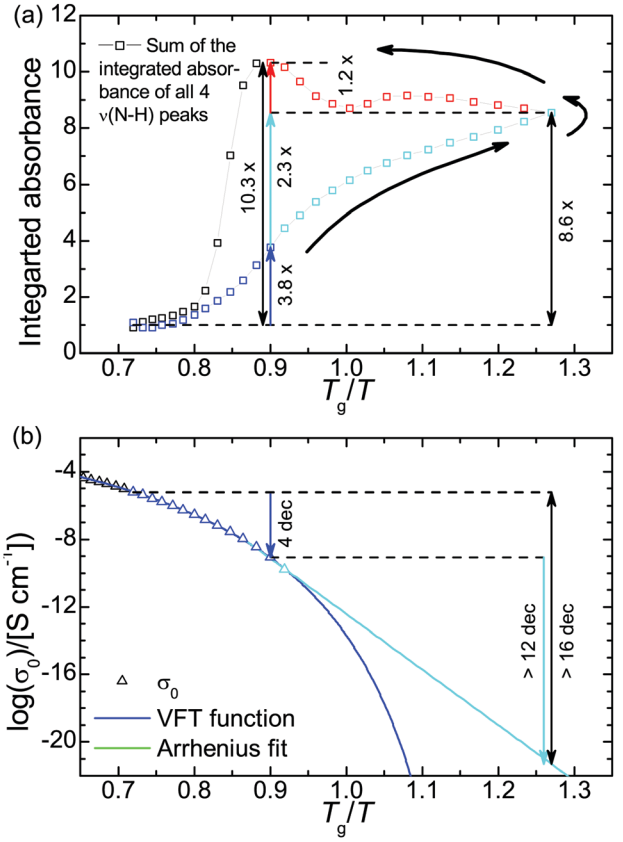

Fig. 5 (a) Cumulative integrated absorbance of ν(N–H) and (b) DC-conductivity. The DC-conductivity during heating is not shown since the hysteresis ($\Delta \log(\sigma') = -0.10$, eqn (5)) is too small to be visible in this plot. Please note, the integrated absorbance is normalized to 1 at 300 K. The relative uncertainty is equal or less than 2% and hence smaller than the symbol size. The logarithm in panel b is to base 10.

During step 1, the number density of H-bonds increases by a factor of 3.8. At the same time the DC-conductivity is reduced by 4 orders of magnitude (Fig. 5). In step 2, the DC-conductivity decreases further by more than 12 orders of magnitude (extrapolated from a conservative Arrhenius fit), while the H-bond density increases only to the 8.6-fold of the initial value or by a factor of 2.3 compared to the value at 240 K. Already at this position within the temperature cycle it is evident that the increase in H-bond density during the first step (factor 3.8) is bigger than during the second one (factor 2.3), whereas the change in DC-conductivity is bigger during the second temperature change (4 orders of magnitude *vs.* 12). This finding further supports the perception of glassy dynamics assisted hopping. We note, that the chosen Arrhenius dependence for extrapolating the thermal activation of the DC-conductivity marks a very upper limit of σ_0; most likely, its value will be much lower leading to a much bigger reduction of σ_0 during step 2. In general, the thermal activation of the conductivity in polyILs changes from a Vogel–Fulcher–Tammann- (VFT) into an Arrhenius-dependence at a particular temperature T_{σ_0}, which is frequently reported to coincide with T_g[21,22] but can be very distinct as recently published.[32]

During step 3, the number density of H-bonds increases further to the 10.3-fold of the initial value (a factor of 1.2 more than compared to their density at 170 K); the DC-conductivity, instead, increases approximately by about the same amount as it was reduced during step 2, except for a residue of 20% ($\Delta \log_{10}(\sigma') = -0.10$, eqn (5)).

At the first glance, the heating run increases the H-bond density even further, whereas the conductivity rises as well. Obviously, the conductivity is generally dominated by the thermal activation of molecular fluctuations, rather than by H-bonding.

In a more detailed view, the conductivity rises (because of thermal activation) but does not reach the values which were evident during the cooling run at the same temperatures. Because the thermal activation of molecular fluctuations is identical at the same absolute temperatures, reduced conductivity in step 3 must arise from the increased H-bond density (as evidenced by means of IR spectroscopy). We can conclude for the particular case of PAAPS that H-bonding hinders molecular fluctuations and hence charge transport hopping.

We are aware that the current results contradict the frequently published concept of fast proton hopping within hydrogen bond networks, which is believed to be faster than structural fluctuations.[17,18,36] One indication for fast proton or synonymously superionic conduction is the DC-conductivity at T_g with the limit of 10^{-15} S cm^{-1}.[18,36] In the case of the polyIL PAAPS, σ_0 amounts 2.1×10^{-14} S cm^{-1} at T_g, which is comparable with recently published low molecular weight proton conductors as lidocaine-hemisuccinate or lidocaine-dihydrogen citrate ($\sigma_0 = 3.7 \times 10^{-14}$ or 1.6×10^{-13} S cm^{-1}, respectively).[36] However, the combination of IR spectroscopy and BDS together with temperature cycling provides findings that object the concept of fast proton hopping. The results by Davidowski *et al.*[63] as well as the one by FTIR and NMR spectroscopy and DFT simulations corroborate the non-complete ionization state of donor and acceptor, which is believed to be favorable for proton conduction.[36]

In addition, FTIR spectroscopy reveals that the number density of H-bonds is drastically increased during cooling and even further increased during subsequent heating (hysteresis in Fig. 5a). Since a higher H-bond density is believed to favor proton conductivity,[36] in the hypothetical case of fast proton conduction the DC-conductivity would be expected to be greater, when the H-bond density is increased at the same particular temperature. This is not the case for PAAPS; at the same temperature the DC-conductivity is reduced with increased H-bond density.

Even though PAAPS fulfills the prerequisites for fast proton hopping, such as sufficiently high ΔpK_a for proton transfer but delocalized protons and an increased H-bond density,[36] we have to conclude that for our protic polyIL the charge transport is mediated through a hopping mechanism which is not dominated by fast proton hopping. Instead, the hopping mechanism is governed by structural fluctuations, which obey glassy dynamics and are hindered through H-bonding (Fig. 6).

5 Conclusion

On the basis of IR spectroscopy, we prove the formation of an extended H-bond network in the protic polymerized ionic

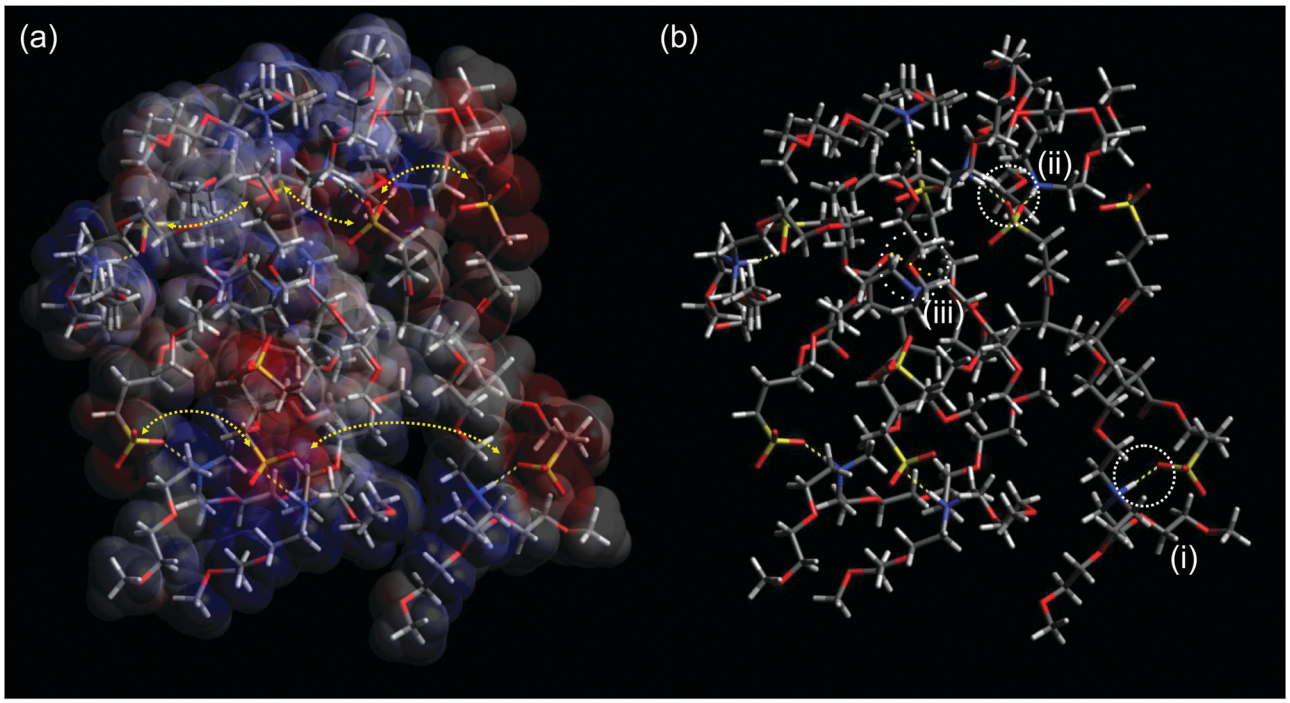

Fig. 6 (a) Surface charge of a PAAPS oligomer (8 repeat units) surrounded by 8 cations (blue: positive; red: negative; gray: neutral) and schematic representation of hopping conduction of transient dipole moments between ammonium moieties of the cations and sulfonate groups at the outermost ends of the polymer side chains. Because the fluctuations of transient dipole moments are dominated by the thermally activated fluctuations of the molecular moieties as described in the framework of glass transition-assisted hopping, the conductivity obeys a VFT-dependence.[31] Moreover, hydrogen bonding hinders the molecular mobility which becomes evident in a reduced conductivity at the same temperature but increased H-bond density (Fig. 2b); (b) hydrogen bonding scenarios as recorded *via* FTIR spectroscopy: (i) H-bond between one oxygen atom of the sulfonate group and one ammonium part or (ii) between two different oxygen atoms of one sulfonate group and two different ammonium parts, as indicated by the measured spectral blue shift (Fig. 2c) and the blue shift in simulations from Huang *et al.*[48] (iii) H-bond formation between carboxyl and ammonium groups might be possible; however, the carboxyl group is effectively screened from interactions and only 11% of all groups undergo inter- as well as intra-molecular interactions (*cf.* ESI†). Please note this structure is for visualization purposes only. The system was constructed by adding 8 monomers forming one main chain and 8 cations in arbitrary order and allowed to relax without any constraints in accord to the Merck molecular force field 94 (MMFF94)[71] following the steepest decent in Avogadro molecule editor program.[72]

liquid PAAPS. This network is in accordance with ^{1}H chemical shift, which indicates an intermediate bound state of the proton between donor and acceptor unit, as stated by Davidowski *et al.*[63] Moreover, when the sample is heated after previous cooling during the temperature cycle, the network becomes even more strengthened giving rise to a pronounced hysteresis. Because of the extremely low cooling/heating rate of 0.012 K s^{-1}, which corresponds approximately to the structural relaxation rate at T_g of 10^2 s,[31,32] the system is able to follow temperature changes above T_g; a too fast cooling/heating as cause for this hysteresis is excluded.

On the basis of broadband dielectric spectroscopy (BDS), we record the conductivity during the temperature cycles and determine two attributes. First, cooling and heating affect the DC-conductivity by several orders of magnitude, as frequently observed for hopping transport.[25,31,32,73] Second, at the same temperature σ_0 differs for different H-bond densities; a (by a factor of 3) greater density results in (20%) lower conductivity. Thus, for the particular case of PAAPS it is demonstrated that the thermal activation of molecular fluctuations affects the charge transport to a much greater extent than H-bonding. Furthermore, at the identical temperature and identical thermal activation an increased H-bond density reduces the conductivity.

This very first study combining FTIR spectroscopic and BDS measurements during temperature cycling in order to investigate H-bond formation in protic polyILs provides detailed results about moiety-specific H-bonding and macroscopic conductivity as well as their interrelation. The sample under study provides the second highest published DC-conductivity at 300 K for anhydrous polyIL;[31] interestingly, the anhydrous polyIL with the highest published DC-conductivity at 300 K has similar elements in its chemical structure.[37] Thus, in the frame of these results the concept of charge transport in this class of materials may need to be reshaped. The DC-conductivity might be adjusted *via* T_g reduction, whereas mechanical properties can be customized *via* H-bond density on a much less expense of conductivity.

Conflicts of interest

There are no conflicts to declare.

Acknowledgements

A. M. A. thanks the Deutsche Forschungsgemeinschaft (DFG) for financial support of project AN 1523/1-1, A. M. A. and F. K.

for granting project B08 within the framework of SFB/TRR 102, F. F. and F. K. for support of project KR 1138/24-1. M. T. is grateful to the DFG for granting project B15 within the framework of SFB/TRR 102 as well as to the Alexander von Humboldt foundation for granting his Feodor-Lynen postdoc fellowship. J. Y. is grateful for financial support from the ERC Starting Grant NAPOLI-639720, the Swedish Research Council (Project No. 2018-05351), and the Wallenberg Academy Fellow program (KAW 2017.0166).

References

1 X. Wang, Y. Chi and T. Mu, *J. Mol. Liq.*, 2014, **193**, 262–266.
2 S. Aparicio, M. Atilhan and F. Karadas, *Ind. Eng. Chem. Res.*, 2010, **49**, 9580–9595.
3 M. Armand, F. Endres, D. R. MacFarlane, H. Ohno and B. Scrosati, *Nat. Mater.*, 2009, **8**, 621–629.
4 K. Ghandi, *Green Sustainable Chem.*, 2014, **4**, 44–53.
5 H. Ohno and K. Ito, *Chem. Lett.*, 1998, 751–752.
6 H. Ohno, M. Yoshizawa-Fujita and Y. Kohno, *Bull. Chem. Soc. Jpn.*, 2019, **92**, 852–868.
7 P. G. Jessop, D. J. Heldebrant, X. Li, C. A. Eckert and C. L. Liotta, *Nature*, 2005, **436**, 1102.
8 S. G. Cull, J. D. Holbrey, V. Vargas-Mora, K. R. Seddon and G. J. Lye, *Biotechnol. Bioeng.*, 2000, **69**, 227–233.
9 D. Langevin, Q. T. Nguyen, S. Marais, S. Karademir, J.-Y. Sanchez, C. Iojoiu, M. Martinez, R. Mercier, P. Judeinstein and C. Chappey, *J. Phys. Chem. C*, 2013, **117**, 15552–15561.
10 M. Forsyth, L. Porcarelli, X. Wang, N. Goujon and D. Mecerreyes, *Acc. Chem. Res.*, 2019, **52**, 686–694.
11 S. Menne, J. Pires, M. Anouti and A. Balducci, *Electrochem. Commun.*, 2013, **31**, 39–41.
12 S. Schneider, T. Hawkins, Y. Ahmed, M. Rosander, L. Hudgens and J. Mills, *Angew. Chem., Int. Ed.*, 2011, **50**, 5886–5888.
13 T. L. Greaves and C. J. Drummond, *Chem. Rev.*, 2008, **108**, 206–237.
14 A. Bagno, C. Butts, C. Chiappe, F. D'Amico, J. C. D. Lord, D. Pieraccini and F. Rastrelli, *Org. Biomol. Chem.*, 2005, **3**, 1624–1630.
15 J. A. Widegren, A. Laesecke and J. W. Magee, *Chem. Commun.*, 2005, 1610–1612.
16 M. Anouti, A. Vigeant, J. Jacquemin, C. Brigouleix and D. Lemordant, *J. Chem. Thermodyn.*, 2010, **42**, 834–845.
17 Z. Wojnarowska, H. Feng, M. Diaz, A. Ortiz, I. Ortiz, J. Knapik-Kowalczuk, M. Vilas, P. Verdia, E. Tojo, T. Saito, E. W. Stacy, N.-G. Kang, J. W. Mays, D. Kruk, P. Wlodarczyk, A. P. Sokolov, V. Bocharova and M. Paluch, *Chem. Mater.*, 2017, **29**, 8082–8092.
18 Z. Wojnarowska, J. Knapik, M. Díaz, A. Ortiz, I. Ortiz and M. Paluch, *Macromolecules*, 2014, **47**, 4056–4065.
19 J. R. Nykaza, Y. Ye, R. L. Nelson, A. C. Jackson, F. L. Beyer, E. M. Davis, K. Page, S. Sharick, K. I. Winey and Y. A. Elabd, *Soft Matter*, 2016, **12**, 1133–1144.
20 M. H. Allen, S. Wang, S. T. Hemp, Y. Chen, L. A. Madsen, K. I. Winey and T. E. Long, *Macromolecules*, 2013, **46**, 3037–3045.
21 U. H. Choi, Y. Ye, D. S. de la Cruz, W. Liu, K. I. Winey, Y. A. Elabd, J. Runt and R. H. Colby, *Macromolecules*, 2014, **47**, 777–790.
22 C. Iacob, A. Matsumoto, M. Brennan, H. Liu, S. J. Paddison, O. Urakawa, T. Inoue, J. Sangoro and J. Runt, *ACS Macro Lett.*, 2017, **6**, 941–946.
23 C. Tracy, A. M. Adler, A. Nguyen, R. D. Johnson and K. M. Miller, *ACS Omega*, 2018, **3**, 13442–13453.
24 E. Mapesa, M. Chen, M. F. Heres, M. A. Harris, T. Kinsey, Y. Wang, T. E. Long, B. S. Lokitz and J. R. Sangoro, *Macromolecules*, 2019, **52**, 620–628.
25 F. Frenzel, W. H. Binder, J. R. Sangoro and F. Kremer, in *Dielectric Properties of Ionic Liquids*, ed. M. Paluch, Springer International Publishing, 2016, ch. Glassy Dynamics and Charge Transport in Polymeric Ionic Liquids, pp. 115–129.
26 J. R. Sangoro and F. Kremer, *Acc. Chem. Res.*, 2012, **45**, 525–532.
27 J. R. Sangoro, C. Iacob, A. L. Agapov, Y. Wang, S. Berdzinski, H. Rexhausen, V. Strehmel, C. Friedrich, A. P. Sokolov and F. Kremer, *Soft Matter*, 2014, **10**, 3536–3540.
28 J. R. Sangoro, C. Iacob, W. K. Kipnusu, M. Jasiurkowska, R. Valiullin, C. Friedrich, J. Kärger and F. Kremer, *Soft Matter*, 2011, **7**, 10565–10568.
29 J. R. Sangoro, C. Iacob, S. Naumov, R. Valiullin, H. Rexhausen, J. Hunger, R. Buchner, V. Strehmel, J. Kärger and F. Kremer, *Soft Matter*, 2011, **7**, 1678–1681.
30 J. R. Sangoro, M. Mierzwa, C. Iacob, M. Paluch and F. Kremer, *RSC Adv.*, 2012, **2**, 5047–5050.
31 F. Frenzel, R. Guterman, A. M. Anton, J. Yuan and F. Kremer, *Macromolecules*, 2017, **50**, 4022–4029.
32 F. Frenzel, P. Borchert, A. M. Anton, V. Strehmel and F. Kremer, *Soft Matter*, 2019, **15**, 1605–1618.
33 C. Gainaru, E. W. Stacy, V. Bocharova, M. Gobet, A. P. Holt, T. Saito, S. Greenbaum and A. P. Sokolov, *J. Phys. Chem. B*, 2016, **120**, 11074–11083.
34 E. W. Stacy, C. P. Gainaru, M. Gobet, Z. Wojnarowska, V. Bocharova, S. G. Greenbaum and A. P. Sokolov, *Macromolecules*, 2018, **51**, 8637–8645.
35 S. Prescher, F. Polzer, Y. Yang, M. Siebenbürger, M. Ballauff and J. Yuan, *J. Am. Chem. Soc.*, 2014, **136**, 12–15.
36 Z. Wojnarowska, K. J. Paluch, E. Shoifet, C. Schick, L. Tajber, J. Knapik, P. Wlodarczyk, K. Grzybowska, S. Hensel-Bielowka, S. P. Verevkin and M. Paluch, *J. Am. Chem. Soc.*, 2015, **137**, 1157–1164.
37 A. Jourdain, A. Serghei and E. Drockenmuller, *ACS Macro Lett.*, 2016, **5**, 1283–1286.
38 J. C. Dyre, *J. Appl. Phys.*, 1988, **64**, 2456–2468.
39 T. B. Schröder and J. C. Dyre, *Phys. Rev. Lett.*, 2000, **84**, 310–313.
40 *Broadband Dielectric Spectroscopy*, ed. F. Kremer and A. Schönhals, Springer-Verlag Berlin Heidelberg GmbH, Berlin Heidelberg New York, 1st edn, 2003.
41 W. H. T. Davison, *J. Chem. Soc.*, 1955, 3270–3274.
42 T. Miyazawa, K. Fukushima and Y. Ideguchi, *J. Chem. Phys.*, 1962, **37**, 2764–2776.
43 K.-J. Liu and J. L. Parsons, *Macromolecules*, 1969, **2**, 529–533.

44 M. A. K. L. Dissanayake and R. Frech, *Macromolecules*, 1995, **28**, 5312–5319.
45 D. H. Johnston and D. F. Shriver, *Inorg. Chem.*, 1993, **32**, 1045–1047.
46 A. G. Bishop, D. R. MacFarlane, D. McNaughton and M. Forsyth, *J. Phys. Chem.*, 1996, **100**, 2237–2243.
47 R. Frech, S. Chintapalli, P. G. Bruce and C. A. Vincent, *Macromolecules*, 1999, **32**, 808–813.
48 W. Huang, R. Frech and R. A. Wheeler, *J. Phys. Chem.*, 1994, **98**, 100–110.
49 K. Haupa, A. Bil and Z. Mielke, *J. Phys. Chem. A*, 2015, **119**, 10724–10734.
50 V. H. Paschoal, L. F. O. Faria and M. C. C. Ribeiro, *Chem. Rev.*, 2017, **117**, 7053–7112.
51 H. Matsuura and T. Miyazawa, *Bull. Chem. Soc. Jpn.*, 1967, **40**, 85–94.
52 R. Pruthtikul, M. M. Coleman, P. C. Painter and N. B. Tan, *Macromolecules*, 2001, **34**, 4145–4150.
53 Y. Mikhaylova, G. Adam, L. Häussler, K.-J. Eichhorn and B. Voit, *J. Mol. Struct.*, 2006, **788**, 80–88.
54 G. Socrates, *Infrared and Raman Characteristic Group Frequencies: Tables and Chartes*, John Wiley & Sons, Ltd, Chichester, 3rd edn, 2004.
55 G. R. Desiraju and T. Steiner, *The Weak Hydrogen Bond In Structural Chemistry and Biology*, Oxford University Press, Oxford New York, 1st edn, 2001.
56 Q.-G. Zhang, N.-N. Wang and Z.-W. Yu, *J. Phys. Chem. B*, 2010, **114**, 4747–4754.
57 R. Hayes, S. Imberti, G. G. Warr and R. Atkin, *Angew. Chem., Int. Ed.*, 2013, **52**, 4623–4627.
58 A. V. Iogansen, *Spectrochim. Acta, Part A*, 1999, **55**, 1585–1612.
59 A. D. Sherry and K. F. Purcell, *J. Am. Chem. Soc.*, 1972, **94**, 1848–1853.
60 Z. Wojnarowska and M. Paluch, *J. Phys.: Condens. Matter*, 2015, **27**, 073202.
61 J.-P. Belieres and C. A. Angell, *J. Phys. Chem. B*, 2007, **111**, 4926–4937.
62 D. R. MacFarlane, J. M. Pringle, K. M. Johansson, S. A. Forsyth and M. Forsyth, *Chem. Commun.*, 2006, 1905–1917.
63 S. K. Davidowski, F. Thompson, W. Huang, M. Hasani, S. A. Amin, C. A. Angell and J. L. Yarger, *J. Phys. Chem. B*, 2016, **120**, 4279–4285.
64 K. Nakamoto, M. Margoshes and R. E. Rundle, *J. Am. Chem. Soc.*, 1955, **77**, 6480–6486.
65 F. Neese, *Wiley Interdiscip. Rev.: Comput. Mol. Sci.*, 2012, **2**, 73–78.
66 W. J. Hehre, R. Ditchfield and J. A. Pople, *J. Chem. Phys.*, 1972, **56**, 2257–2261.
67 M. M. Francl, W. J. Pietro, W. J. Hehre, J. S. Binkley, M. S. Gordon, D. J. DeFrees and J. A. Pople, *J. Chem. Phys.*, 1982, **77**, 3654–3665.
68 V. A. Rassolov, J. A. Pople, M. A. Ratner and T. L. Windus, *J. Chem. Phys.*, 1998, **109**, 1223–1229.
69 F. Neese, M. Atanasov, G. Bistoni, D. Maganas and S. Ye, *J. Am. Chem. Soc.*, 2019, **141**, 2814–2824.
70 J. R. Sangoro, C. Iacob, A. Serghei, C. Friedrich and F. Kremer, *Phys. Chem. Chem. Phys.*, 2009, **11**, 913–916.
71 T. A. Halgren, *J. Comput. Chem.*, 1996, **17**, 490–519.
72 M. D. Hanwell, D. E. Curtis, D. C. Lonie, T. Vandermeersch, E. Zurek and G. R. Hutchison, *J. Cheminf.*, 2012, **4**, 17.
73 F. Frenzel, M. Y. Folikumah, M. Schulz, A. M. Anton, W. H. Binder and F. Kremer, *Macromolecules*, 2016, **49**, 2868–2875.